4 Spin-polarized Scanning Tunneling Microscopy

Wulf Wulfhekel · Uta Schlickum · Jürgen Kirschner

Summary. We give an introduction to spin-polarized scanning tunneling microscopy (Sp-STM), a magnetic imaging technique with nanometer lateral resolution. Sp-STM allows to record constant current images which represent the electron density near the sample surface and simultaneously the spin polarization of the electron density which is related to the magnetic moment. It is shown how magnetic and topographic information can be separated using a modulation technique of the magnetization of bulk ferromagnetic tips. It is demonstrated that the out-of-plane component as well as one well-defined in-plane component of the spin polarization can be recorded. Finally, it is shown that with Sp-STM valuable information on the spin-resolved electronic structure and on the fundamental processes of tunneling spins may be obtained.

4.1 Introduction

The imaging of magnetic domains in small structures is one of the important basis of modern micro-magnetism. While the existence of magnetic domains was initially not directly shown with an imaging technique, but was deduced from the observation of discontinuous jumps in the hysteresis loops [1], magnetic imaging has become the method of choice when investigating the magnetic structure. Since the early works of Barkhausen, several magnetic imaging techniques, i.e. techniques that map one or more components of the magnetization or related quantities were developed. The measured quantity can be e.g. the magnetic vector potential, the magnetization, the magnetic stray field or the spin polarization. We here focus on spin-polarized scanning tunneling microscopy (Sp-STM), which maps the spin polarization of a conductive sample surface.

4.1.1 The Resolution Problem in Magnetic Imaging

In modern applications, e.g. magnetic recording media or magnetic random access memory, the size of the magnetic structures or domains is in the range of several 10 nm and the trend of miniaturization is still holding on. This poses some severe resolution problems to most established magnetic imaging techniques. For example, magnetic force microscopy (MFM) is intrinsically limited in lateral resolution by the physical effect used to obtain magnetic contrast. MFM relies on the long range magnetic dipolar interaction of a magnetic tip and the magnetic charges of the sample. To obtain reasonable forces, the magnetic volume of the tip has to be of sufficient

size. Further, the magnetic tip has to be lifted several nm above the surface to avoid other interactions like the van-der-Waals force to cover up the small magnetostatic forces. These constrains in localization of the interaction lead to a limit of the MFM resolution around several 10 nm [2]. Resolution limits of similar size exists for most other magnetic imaging techniques. More details on this can be found in [2]. To further develop new magnetic recording media, alternative magnetic imaging techniques are required.

In fundamental studies of magnetism, there exists a similar need for high resolution magnetic imaging. Many fundamental questions in magnetism are linked to processes that operate on the atomic scale and are beyond the lateral resolution of the established techniques. At the forefront of nano-science, high resolution imaging techniques are in general of high interest and impact. Sp-STM may contribute substantially in the study of magnetism on the nanometer scale, as its resolution is given by the lateral extension of the tip area that contributes to the tunneling process. Under favorable conditions, this may lead to sub-nanometer lateral resolution [3,4]. We illustrate the capabilities of this new technique and compare it to MFM.

4.1.2 Magnetism and Spin

The key to Sp-STM lies in the relation of magnetism and the electronic structure of matter. In ferromagnets, the spin sensitive exchange interaction between localized electrons (Heisenberg model) or electrons in a delocalized electron gas (Stoner model) splits the electronic density of states into minority and majority densities (see Fig. 4.1a). This is in contrast to paramagnetic substances, where the distributions of spin-up and spin-down electrons are identical. In ferromagnets, the spin splitting leads to an imbalance of the total occupation of the electrons of different spins and as a consequence to the magnetic moment of the atom. The direction of magnetization of the ferromagnet is in general collinear to the direction of the spin polarization, which relates the magnetization to the spin polarization. A measurement of one or more of the components of the spin polarization can give information on one or more components of the direction of magnetization, respectively.

4.1.3 The Tunneling Magnetoresistance Effect

The splitting of the density of states has immediate consequences on the tunneling current. Pioneering field-emission experiments with ferromagnetic tips have shown [5,6] that during the tunneling process from the tip into the vacuum, the spin polarization of the density of states of the tip is partly transferred to the emitted electrons. A spin-polarized current was observed. This can easily be understood on basis of Fermi's golden rule. The tunneling process itself, i.e. the transmission probability through the potential step of the work function in front of the tip, is not spin dependent. The observed polarization is just a consequence of the different number of states for minority and majority electrons: the more states are allowed to tunnel, the higher the resulting tunneling current. In this simplified picture, the tunneling

current from a spin-polarized tip is spin-polarized according to the imbalance of electrons with spin-up and spin-down.

Jullière discovered that when electrons tunnel between two ferromagnets, not only the current is spin-polarized but also the size of the current is influenced [7]. In his experiment, two magnetic films were separated by an insulator film to form a planar tunnel junction. The two magnetic films were chosen to have different coercive fields. This permitted to align their magnetization parallel or antiparallel as a function of an applied magnetic field. Jullière found that the tunneling conductance G (and by this the resistance) depends on the relative orientation of the magnetization of the two layers. This effect is called the tunneling magnetoresistance (TMR) effect. For parallel orientation G was higher than for antiparallel orientation. This finding can be explained on basis of a simple model. As above, we neglect any spin dependence in the transmission through the barrier and focus solely on the density of states of the two electrodes. Under the assumption of a small bias voltage across the junction and in the absence of spin-flip scattering, the electrons in the ferromagnets near the Fermi energy determine the tunneling conductance. For parallel orientation, the majority/minority electrons of the first electrode tunnel into the majority/minority states in the second electrode, respectively, as sketched in Fig. 4.1b. Using Fermi's golden rule, the conductance G is proportional to the density N of initial (i) and final (f) states at the Femi edge. Combining both spin channels, the conductance for parallel oriented magnetizations is given by:

$$G_{\uparrow\uparrow} \propto N^i_{\uparrow} N^f_{\uparrow} + N^i_{\downarrow} N^f_{\downarrow} \tag{4.1}$$

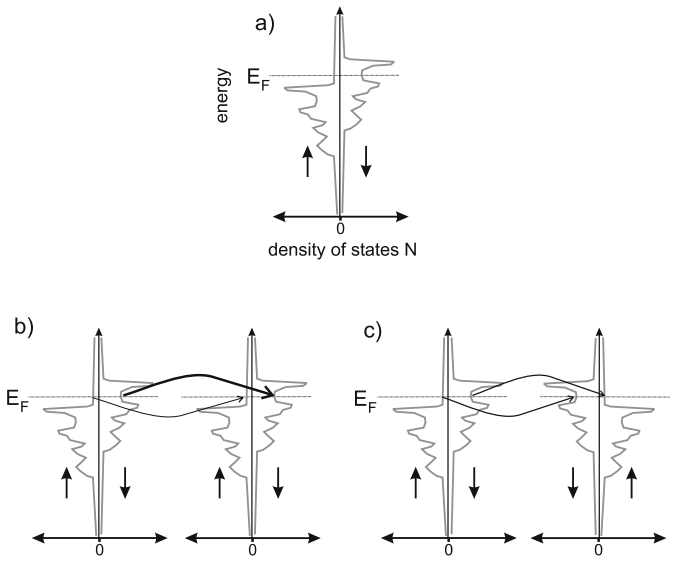

Fig. 4.1. (**a**) Spin-split density of states N of a ferromagnet. $\uparrow/\downarrow$ indicate majority/minority states. (**b**), (**c**) Tunneling between two ferromagnetic electrodes. In (**b**) respectively (**c**) the magnetization of the two electrodes is parallel respectively antiparallel. The conductivities G for tunneling from the *left* to the *right* electrode are indicated by *arrows*

For antiparallel orientation (see Fig. 4.1c), electrons of majority character in one electrode tunnel into states of minority character in the other electrode and the conductance is given by a mixed product:

$$G_{\uparrow\downarrow} \propto N^i_{\uparrow} N^f_{\downarrow} + N^i_{\downarrow} N^f_{\uparrow} \tag{4.2}$$

These two conductivities in general differ leading to a variation of the tunneling current with the relative direction of magnetization of the electrodes. Later, Slonczewski treated the problem of spin-polarized tunneling more rigorously [8]. Neglecting higher order spin effects like spin accumulation, he calculated the dependence of G on the angle θ between the magnetization of the two electrodes. With the spin polarization $P = (N_{\uparrow} - N_{\downarrow})/(N_{\uparrow} + N_{\downarrow})$, and neglecting barrier effects, the conductance is given by:

$$G = G_0(1 + P^i P^f \cos\theta) \tag{4.3}$$

Slonczewski's calculations for the angular dependence of the TMR effect was later experimentally confirmed [9].

In general, if a finite bias is applied, all states between the two Fermi levels are involved in tunneling. They have to be weighted according to their tunneling probability, which is among other things energy dependent. This scenario is more complex but G can be expressed using effective, i.e. correctly weighted, densities or polarizations. More details on this will be given in Sect. 4.6.1.

4.2 The Principle of Spin-polarized Scanning Tunneling Microscopy

With the invention of STM, Binning et al. realized an imaging technique with a lateral resolution that is capable to resolve single atoms [10, 11]. In STM, the apex of a conductive tip is placed near the surface of a conductive sample. Between sample and tip, a bias voltage is applied and a small tunneling current flows, that exponentially decays with tip sample separation. In the constant current mode of STM, a feed back mechanism adjusts the tip sample distance such that a constant tunneling current is obtained. When the tip is scanned over the surface, the tip apex moves on lines of constant current. In the simplest model, these lines are related to lines of constant density of states, i.e. reflect the sample topography. Already in 1988, Pierce suggested to set up a STM that uses the TMR effect to image simultaneously the sample magnetization [12]. All that is needed in addition to convential STM is a spin-polarized tunneling current. He suggested two different approaches to Sp-STM. Besides the obvious use of ferromagnetic, i.e. spin polarized tips, he discussed the possibility to photo-excite spin-polarized carriers in GaAs tips. The latter was realized by Suzuki et al. [13]. In their approach, circularly polarized light was used to excite spin-polarized carriers into the conduction band of the tip that then tunnel into the sample. The spin polarization of the electrons can be selected by the helicity of the light. By modulating the helicity, modulations in the tunneling current were induced due to spin dependent tunneling. The modulations were detected with a lock-in amplifier to separate spin information from topographic information. The success of

this approach was limited. It suffered from a rather low contrast and an unintended additional magneto-optical contrast of low lateral resolution. In this chapter, we focus on Sp-STM experiments with ferromagnetic tips. This approach was more successful. In the pioneering publication of Pierce, three different imaging modes of Sp-STM were suggested. All have been realized experimentally and are briefly explained below. We will, however, focus on only one of the three imaging modes. A detailed description of all imaging modes was given recently, elsewhere [14].

4.2.1 The Constant Current Mode

In the constant current mode, STM images are taken with non magnetic and ferromagnetic tips and the results are carefully compared. Wiesendanger et al. were the first to report results obtained with this mode [15] on the layer-wise antiferromagnetic Cr(001) surface [16]. Using tungsten tips, topographic constant current line-scans revealed atomic steps on Cr(001) of the expected step height of 0.14 nm while using a ferromagnetic CrO_2 tip, alternating step heights of 0.16 and 0.12 nm were observed. This was attributed to the TMR effect between the ferromagnetic tip and the ferromagnetically ordered Cr atoms on the terraces. When the spin polarizations of the tip and the Cr terrace atoms are parallel, the tunneling current is enhanced due to the TMR effect (see (4.3)) and in the constant current mode of the STM, the tip is retracted by a small amount (0.02 nm). On the adjacent atomic terrace on Cr, the spin polarization of the terrace atoms is opposite due to the topological antiferromagnetic order of Cr(001) [16]. Therefore, on this terrace the TMR effect leads to a reduction of the current and the STM tip approaches slightly. This mechanism results in alternating step heights seen with a spin-polarized tip. However, no separation of topography and spin information could be obtained in this imaging mode and reference measurements had to be acquired with non-magnetic tips.

4.2.2 The Spectroscopic Mode

The spectroscopic mode of Sp-STM allows under certain circumstances the separation of topographic information from spin information. This mode is also named spin-polarized scanning tunneling spectroscopy (Sp-STS). It was initially suggested by Pierce [12] and Stroscio et al. [17] and was first realized by Bode et al. [18]. It uses the fact that the spin polarization of the tunneling current is a function of the energy, i.e. the spin polarization of the states that contribute to tunneling depends on the sample bias. For example, when a finite negative sample bias U is applied between tip and sample, in principle the occupied sample states in the range of width U below the Fermi level of the sample contribute to the tunneling. In the tunneling process, the electrons tunnel into the unoccupied tip states of the range U above the Fermi level of the tip. The spin polarization of both the tip and the sample states contribute to the tunneling. Therefore the spin polarization of the tunneling current in general varies with sample bias. To illustrate the mode of operation, let us assume that the spin polarization increases with U. When the magnetic surface is

imaged, the topographic image contains both information of the electronic density and on the spin, as mentioned above. Any variations of the conductance G due to the TMR effect are compensated by changes in the tip sample distance. In Sp-STS, the feed back loop of the STM is switched of and U is increased. As a consequence, the tunneling current changes. As we have assumed a rising spin polarization, the tunneling current for parallel oriented tip and sample magnetization increases more than for antiparralel orientation. Pierce et al. suggested to vary U significantly. Nevertheless, the imaging mode also works for small modulation of U. In this case, the variations in the tunneling current are proportional to the differential conductance $\mathrm{d}I/\mathrm{d}U$. In the pioneering experiment by Bode et al., the observed peak height of the spin-split surface state of Gd(0001) in laterally resolved $\mathrm{d}I/\mathrm{d}U$ spectra was used to obtain magnetic information [18]. The imaging mode is now widely used. It has the advantage that tips coated with a thin film of a ferromagnet or antiferromagnet can be used so that the magnetic stray field of the tips can be minimized or completely be avoided [19, 20]. The obvious disadvantage is that the $\mathrm{d}I/\mathrm{d}U$ signal in Sp-STS only weakly depends on magnetism. It much stronger depends on general variations of the density of states caused by e.g. compositional, structural or morphological changes of the sample. A more detailed overview on this imaging mode can be found in [2].

4.2.3 Differential Magnetic Imaging Mode

In the differential magnetic imaging mode, a bulk ferromagnetic tip is used whose magnetization is modulated. Due to the TMR effect, these modulations lead to modulations of the tunneling current that are related to the spin polarization of the sample. The basic concept of this mode is directly related to (4.3). In the experiment, a magnetically bistable tip is used. The tip magnetization is periodically switched between the two stable configurations of opposite magnetization. This is equivalent to changing the sign of the spin polarization of the tip apex. In the experimental set-up, the magnetization of the tip is reversed by an alternating current through a small coil that is fixed to the tip. The frequency of the alternating current lies above the cut-off frequency of the feed back loop of the STM [21]. Thus, the feed back loop only detects the averaged tunneling current for the two spin polarizations (positive and negative) of the tip apex. As can easily be seen from (4.3), in the averaged tunneling current $\overline{I} = I_0$ all spin-dependent currents cancel out such that that the constant current image contains no magnetic information. With a phase-sensitive lock-in amplifier, the alternating part of the tunneling current ΔI is detected which is proportional to $P^i P^f \cos\Theta$. It contains all the spin information. This way, topographic and spin information are strictly separated and an image of the spin component along the magnetization axis of the tip can be recorded simultaneously with the topography [21]. The alternating magnetic field induced within the coil has to be large enough to fully reverse the magnetization of the tip. The alternating field, however, also creates induction currents in the tunneling loop. For this reason, in an experiment only soft magnetic materials may be used as tips. Moreover, magnetostriction of the tip during the reversal must be avoided. The early experiments of Johnson et al. suffered from large magnetostriction of the Ni tip, so that no stable magnetic or topographic imaging was possible [22].

4.3 Experimental Set-up

In our experiment, the magnetization of a ferromagnetic electrode is switched by applying a small alternating current to a coil wound around the electrode. The direction of magnetization of the STM electrode is mostly determined by its shape. For imaging the out-of-plane component of the spin polarization, a sharp and pointed tip is used [23]. This is schematically shown in Fig. 4.2a. The alternating magnetic field induced by the coil is large enough to fully reverse the magnetization of the tip. In the tip, the magnetization direction lies always along the tip axis due to the large shape anisotropy. Thus, at the tip apex where the tunneling occurs, the magnetization is perpendicular to the sample surface. To image an in-plane component of the sample spin polarization, a ring is used as a STM electrode [24] as schematically shown in Fig. 4.2b. The magnetic field of the coil switches the ring between the two stable circular magnetic configurations. At the bottom of the ring, the magnetization lies tangential to the ring, i.e., in the surface plane. By choosing the plane in which the ring is oriented, the magnetization direction of the ring is defined and thus the direction of the sensitivity in the surface plane for the measured spin signal is known.

Figure 4.3 shows images of the STM electrodes experimental realization. STM tips for recording the out-of-plane componen of the spin polarization (see Fig. 4.3a) were prepared by electrochemical etching from thin CoFeSiB wires of 130 μm diameter. As etching agent, a dilute mixture of HCl and HF was used that was suspended by surface tension as a thin liquid membrane in a Pt ring during etching. The pH value was tuned such that the formation of silica from the Si in the amorphous wire was prevented. Using low etching currents of the order of 250 μA, pointed tips of cone angles typically between 8 and 15° were created (see bottom of Fig. 4.3a). Due to the large shape anisotropy, a tip magnetization is along the tip axis [25]. The magnetic tips were fixed in a non magnetic shaft around which the coil is wound. The chosen tip material offers extremely low coercivities in the range of 50 μT and negligible magnetostriction (smaller than 10^{-8}). This ensures that during switching of the tip, the magnetostriction in the created domain walls is small enough that virtually all mechanical vibrations are suppressed [25]. With detailed micromagnetic simulations of the tip switching process, the expected magnetostriction could be estimated to be below 10^{-14} m, i.e. is irrelevant in the experiment.

For imaging one in-plane component of the spin polarization, ring shaped STM electrodes of the same CoFeSiB material were used [24]. Figure 4.3b shows an image of a ring of about 2 mm outer diameter and a thickness of 25 μm. The rings

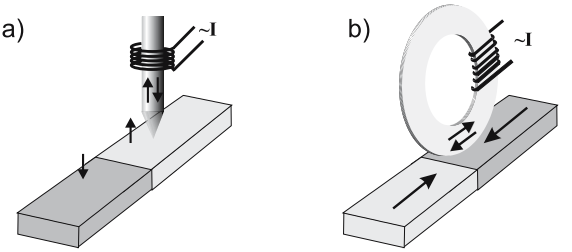

Fig. 4.2. Schematic representation of Sp-STM electrodes for measuring (**a**) the out-of-plane component and (**b**) the in-plane component of the sample spin polarization

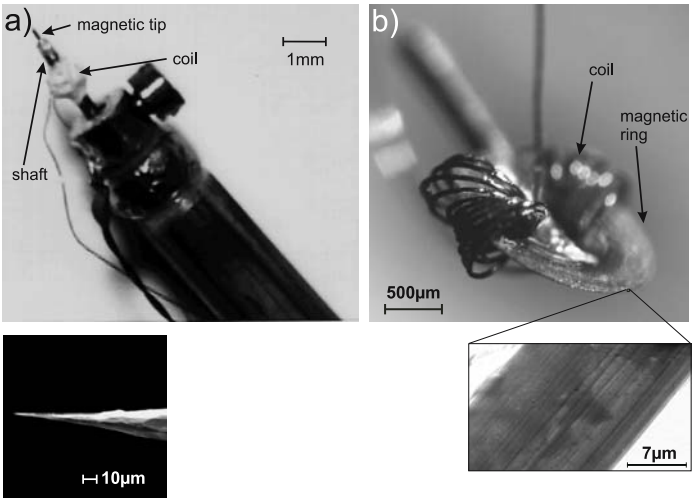

Fig. 4.3. Sp-STM electrodes for measuring (**a**) the out-of-plane component and (**b**) the in-plane component of the sample spin polarization. The zoomed images show scanning electron microscopy images of the pointed end and of the bottom of the ring, respectively

were electrochemically etched from a thin CoFeSiB foil. The coil wound around the ring is clearly visible in Fig. 4.3b. By choosing the ring orientation, the direction of sensitivity in the surface plane is defined. The outer perimeter of the rings were polished to even out the roughness caused by the etching. After polishing, the perimeter is smooth with some minor polishing traces (see bottom of Fig. 4.3b). Although the rings used as STM electrodes are not sharp, a lateral resolution below 1 nm could be achieved [24, 26]. Most likely nano tips exist at the apex which give a high lateral resolution.

To obtain spin contrast, the STM electrodes need to be cleaned in situ by Ar sputtering. The contrast can be increased by coating the CoFeSiB electrodes with several monolayers (ML) of Fe.

4.4 Ferromagnetic Domains and Domain Walls

In this section we give several examples on magnetic domains and domain walls in ferromagnets to illustrate the magnetic imaging capabilities of Sp-STM for the in and out-of-plane components of the magnetization. All studies were carried out in ultra high vacuum and at room temperature. The samples were cleaned by Ar ion etching followed by thermal annealing. The sample surfaces were checked for impurities with Auger electron spectroscopy (AES) and no contaminations could be found within the sensitivity limit of our spectrometer. The crystal structure of the surfaces were check with low energy electron diffraction (LEED). All surfaces showed sharp LEED spots and a low background intensity indicating a single crystalline surface with low concentration of defects.

4.4.1 Ultra-sharp Domain Walls in Co(0001)

When using tips that are magnetized perpendicular to the sample plane, the out-of-plane component of the spin polarization may be imaged [21]. While magnetic stray fields of the tip cannot be avoided in this configuration, hard magnetic samples like hcp Co could be imaged without problems. As an example, the closure domain pattern of Co(0001) is presented. Hcp Cobalt has a uniaxial magetocrystalline anisotropy with an easy direction along the *c*-axis, i.e. perpendicular to the selected (0001) surface. Due to the minimization of the stray field energy, i.e., the net magnetic flux exiting the surface, the single domain state is unstable and splits up into a Lifshitz closure domain pattern. Since for Co the magnetic anisotropy and the dipolar energy are of the same order of magnitude, no perfect and simple closure domain structure occurs on the (0001) surface. Instead, the magnetization of most areas of the surface is strongly rotated away from the surface normal and a dendritic pattern is formed [27]. In the MFM image (see Fig. 4.4a), the complex domain pattern of Co(0001) is visible. The limited lateral resolution of MFM becomes apparent at the magnification of the image. In contrast to MFM, Sp-STM reveals the full detail of the fractal structure as depicted in Fig. 4.4b.

When zooming into the ends of the fractal branches sharp features in the otherwise smooth contrast can be observed as shown in Fig. 4.5a. The contrast across these sharp features resembles domain walls. The observed contrast corresponds, however, not to a 180° domain wall but to an angle of of rotation of only 20°. The width of the transition region between the two domains is only of the order of 1 nm. At first sight, these small widths seem to contradict common knowledge about domain walls. Bloch walls in bulk Co have a width of $\approx$ 11 nm. To exclude instrumental reasons for the observation of such sharp walls, we take the following consideration. A mechanism that often causes artificially sharp walls is a magnetostatic pick-up mechanism in which the domain wall is dragged along with the magnetic tip during scanning until it snaps off. In that case, a sharp transition would be observed at the point of snapping off. To test for this mechanism, we recorded the wall while scanning from the right to the left and from the left to the right (see Fig. 4.5b). If

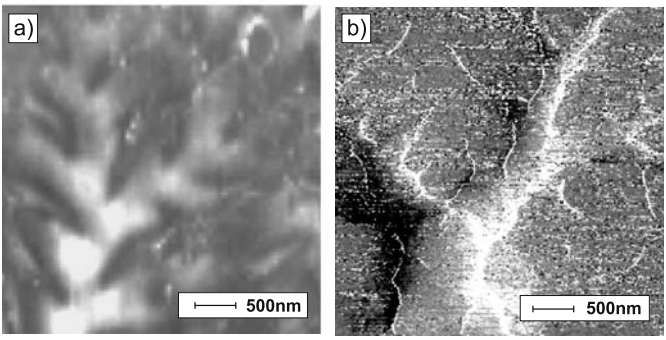

Fig. 4.4. (**a**) MFM and (**b**) Sp-STM image of the fractal domain pattern of Co(0001). The scans were performed on the same sample but not on the same area

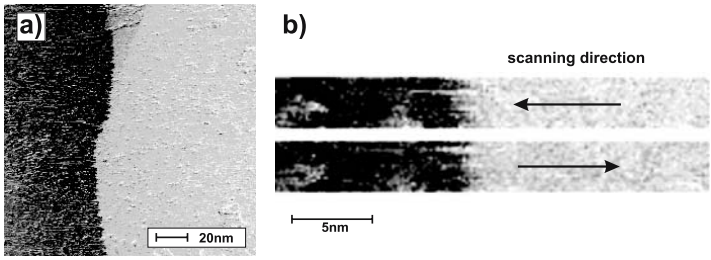

Fig. 4.5. (**a**), (**b**) Sp-STM images of a sharp domain wall on Co(0001). (**b**) No shift in the wall position is observed when inverting the scan direction excluding dragging of the wall

the wall was dragged along and snapped off, opposite displacements of the wall for scanning in the two directions should be seen. The domain wall, however, appears at exactly the same position for both directions ruling out any significant dragging.

To understand the origin of the specific type of 20° wall and to calculate its expected width, we focus on details of the domain pattern of Co(0001). In Co(0001) the magnetocrystalline anisotropy favors a magnetization along the surface normal. To reduce the stray field energy of the sample, domains of opposite magnetization along the normal separated by 180° domain walls are formed in the bulk of the crystal. This magnetization configuration reduces the overall stray field, but still produces a large number of surface charges, since the flux is not kept inside the crystal. As Hubert et al. suggested, the system can reduce the amount of surface charges by a partial flux closure with tilted surface domains [28]. From the ratio between magnetocrystalline and dipolar energy one may calculate the angle θ, the magnetization is tilted from the surface normal. Minimizing the free energy results in a large angle of $\theta \approx 80°$ [23] ,i.e. the flux closure is obtained by almost in-plane magnetized surface domains. Hence, one expects to find 20° domain walls on the surface in agreement with our Sp-STM observations.

To estimate the width of such a 20° domain wall we use a one dimensional model of the domain wall including the magnetic exchange energy and the anisotropy energy of Co [23]. Figure 4.6a shows the wall energy as a function of the wall width w. The minimum energy is found at a wall width of only 1.5 nm. The resulting theoretical wall profile agrees well with the experimentally observed wall profile as depicted

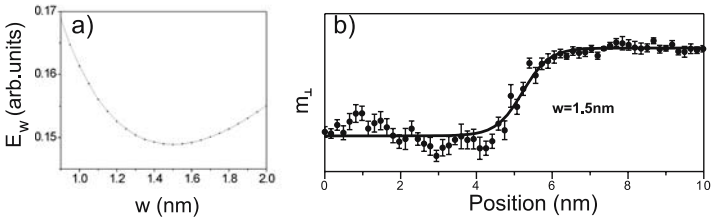

Fig. 4.6. (**a**) Calculated energy of a 20° domain wall in Co(0001) as function of its width. (**b**) Experimental wall profile (*points*) and calculated wall profile (*solid line*) of a 20° domain wall

in Fig. 4.6b. Especially, the experimental wall profile does not appear blurred when compared to the calculated one indicating a lateral resolution better than 1 nm. The experiments illustrate the possibility, that a domain wall may be narrower than the magnetic exchange length of $\sqrt{A/K}$ without violation of micromagnetic rules (A and K are the magnetic exchange constant and the magnetic anisotropy, respectively). This holds since the angle of rotation across the wall is small [23].

4.4.2 Asymmetric Nèel Caps in Fe(001)

Using ring electrodes, the bottom of the ring is magnetized tangential such that the in-plane component of the spin polarization along the ring plane is imaged [24]. In case the ring is perfect, the magnetic flux is closed and no magnetic stray field exits. This allows the imaging of extremely soft magnetic samples. As an example, the Nèel caps in Fe-whiskers were investigated. Fe-whiskers are needle-like Fe single crystals that are terminated by (001) surfaces. The magnetic ground state is the so called Landau state, in which the flux inside the Fe-whisker is closed. The whisker splits up into two elongated domains that are magnetized along the long side of the whisker. The magnetization at the surface of an Fe-whisker lies in-plane. The domains are separated by a 180° domain wall. At the two ends of the whiskers, closure domains are formed. Figure 4.7a shows a magneto optic Kerr effect (MOKE) image of an Fe-whisker taken after sample surface preparation in the UHV chamber. The 180° domain wall along ⟨100⟩ can be seen immediately. The MOKE images were recorded to find the position of the wall such that the ring electrode of the Sp-STM can be placed close to the wall.

Figure 4.7b,c show the topographic and the magnetic Sp-STM images taken at the same time. In the topographic image, flat terraces of several 100 nm width separated by atomic steps are visible. Fe-whisker surfaces are rather flat which is a necessary condition for imaging with a ring as a dull STM electrode. Nevertheless, the ring electrode allows topographic imaging with nm resolution which can be explained by the existance of nano-tips on the outer ring perimeter. In the image of

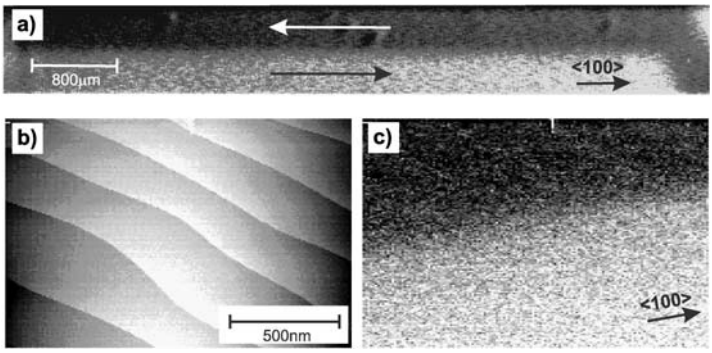

Fig. 4.7. (**a**) Magneto optic Kerr image of an Fe-whisker. (**b**) Topographic and (**c**) spin polarization images recorded simultaneously. The 180° domain wall seen in (**a**) is also clearly visible in (**c**)

the spin signal, clearly two domains separated by a 180° domain wall running along the ⟨100⟩ direction can be seen. The wall is rather wide. This is not caused by the lateral resolution of the instrument but is due to the magnetic properties of Fe.

In the interior of the Fe-whisker, the two domains are separated by a charge free Bloch wall, i.e. the magnetization in the wall rotates in the plane of the wall. At the surface of the whisker, this would lead to an orientation of the wall magnetization perpendicular to the sample plane creating magnetic surface charges. This is energetically unfavorable so that the magnetization of the wall at the surface rotates in the surface plane, i.e. a Néel cap is formed. As has been shown in detailed calculations, the curling of the Bloch wall to a surface Néel cap is asymmetric [29] resulting in an asymmetric wall profile at the surface. In Fig. 4.8, the solid line represents the micromagnetically simulated line profile across the 180° domain wall. It shows the in-plane component of the magnetization pointing along the domain wall. The measured wall profile (squares) perfectly agrees with the calculated data within the lateral calibration error of the scanner ($\approx$ 10%). The agreement between theory and experiment indicates not only that with Sp-STM one may image a well-defined in-plane component of the spin polarization. It also shows that the ring electrode is indeed free of stray fields. Even small fields of the order of 100 μT are sufficient to move the domain walls in whiskers by several μm. As we see practically no blurring in the experimental wall profile when compared to the theoretical profile, the local stray field of the ring have to be significantly below the above mentioned value.

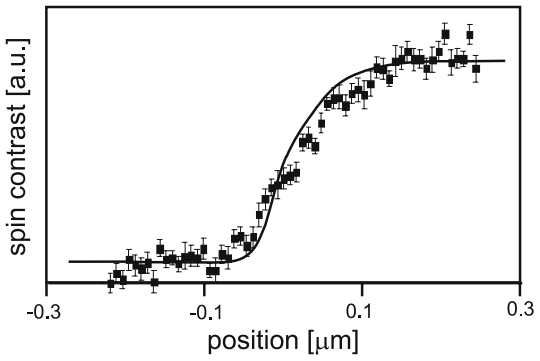

Fig. 4.8. Calculated (*solid*) and measured (*squares*) wall profile across the Néel cap on an Fe-whisker. The calculations were taken from [29]

4.5 Antiferromagnets in Contact with Ferromagnets

Antiferromagnetic surfaces can be investigated as well, as in Sp-STM the spin polarization at the surface is mapped. We here focus on topological antiferromagnets. In these, the magnetic moments within one atomic layer of the crystal couple ferromagnetically while the adjacent layers couple antiferromagentically. In other words: the material is a layered antiferromagnet. We show two examples for these systems which both were grown on Fe(001) as a substrate and both show an in-plane spin polarization.

4.5.1
Mn on Fe(001) and Topologically Induced Frustrations

As a model system for the topological antiferromagnets, we focus on Mn grown on Fe(001). Mn can be stabilized at room temperature in a body centered tetragonal (bct) structure on Fe(001) [30]. The bct structure is stable up to about 20 ML [31–33]. Mn films have an out-of-plane lattice constant of 0.323 nm, i.e. a little larger than the 0.287 nm of Fe. Mn grows in a layer-by-layer mode up to 10 to 20 ML [34]. The critical thickness strongly depends on the substrate quality and the growth temperature. When Mn was deposited at room temperature, no intermixing was found. The onset of intermixing was observed by AES for substrate temperatures above 420 K [33, 38]. In STM studies, interdiffusion of Fe into the first ML Mn was found at substrate temperatures above 370 K [39]. The intermixing was observed until the fourth Mn layer [37]. At the Mn surface of films between 4 to 10 ML, small regions with rectangular cross-shaped patterns start to form [36,37]. It was speculated that these small rectangular islands are local reconstructions and a precursor to three-dimensional growth.

The first evidence that Mn on Fe(001) is a layer-wise antiferromagnet was reported by Walker and Hopster [38]. This was confirmed with scanning electron microscopy with polarization analysis (SEMPA) [34] and later with spin-polarized STM in the spectroscopy mode [20].

Figure 4.9 shows the example of a thin Mn film grown on Fe(001). The topographic image of the Mn film indicates an imperfect layer-by-layer growth as several layers are exposed at the surface. The terraces are separated by single atomic steps as can be deduced from the line scan in Fig. 4.9b. The Fe substrate was homogenously magnetized in one direction over the whole imaged area, as determined by Kerr-microscopy. The direction of sensitivity of the ring was chosen collinear to the magnetization of the Fe substrate. Thus, the imaged spin signal shows the projection of the spin component collinear to the Fe magnetization. The Sp-STM images taken simultaneously to the topographic images show an alternating contrast on the atomic terraces of Mn (see Fig. 4.9c) confirming a layer-wise antiferromagnetic order. In agreement to that, the spin signal is identical on all terraces but the sign alters (see the line scan in Fig. 4.9d).

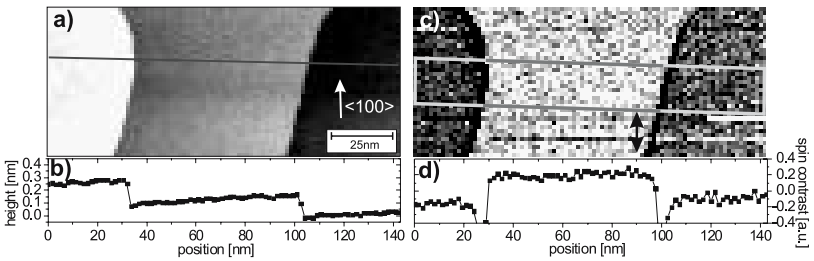

Fig. 4.9. (**a**) Topographic STM image and (**b**) line scan of 7 ML Mn on Fe(001). (**c**) Magnetic Sp-STM image of the same area and (**d**) line scan revealing the layer-wise antiferromagnetic order of bct Mn. The direction of sensitivity for the spin is parallel to the whisker axis and is indicated in (**c**)

This ideal antiferromagnetic order was found on most areas of the Mn film. The unperturbed layer-wise antiferromagnetic order is, however, disturbed in case a step of the underlaying Fe substrate is present. Figure 4.10a presents schematically the topological and magnetic situation of Mn layers overgrowing a step edge of the Fe substrate underneath. The thickness of the Mn layers on both sides of a monatomic Fe step differs by one ML. Due to the vertical lattice mismatch, subatomic steps are formed at the Mn film surface at the position of Fe step edges. The situation of the magnetic order above such step edges is more complicated. An undisturbed layer-wise antiferromagnetic order within the Mn film is not possible when the Mn moments at the interface on both sides of the step edge are aligned in the same direction by the Fe substrate. Instead, Mn layers which meet at the position of the Fe step edge are magnetized oppositely. This leads to a magnetic frustration [40, 41].

Figure 4.10b shows a Sp-STM image of the topography of a Mn film grown over a monatomic step of the Fe substrate. In the topography, a buried Fe step edge is running almost vertically through the center of the imaged area (black arrows as guideline). The line profile in Fig. 4.10c taken along the black line in Fig. 4.10b

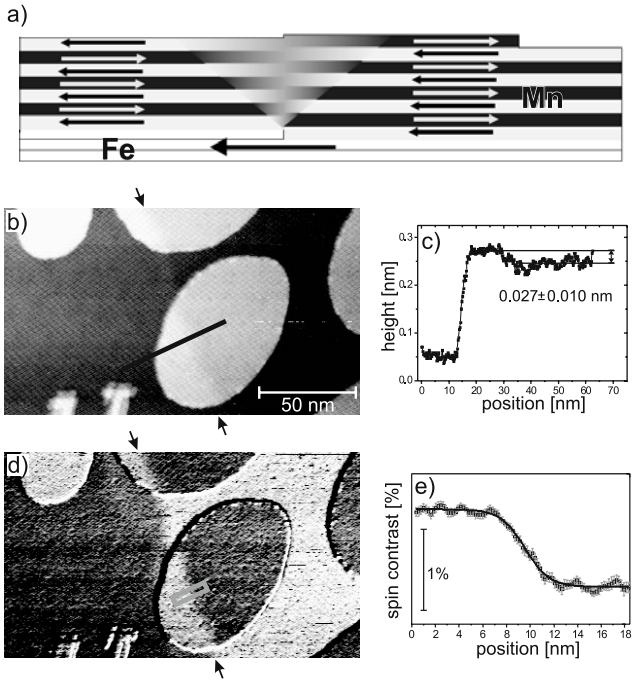

Fig. 4.10. (**a**) Schematic sketch of the topographic and magnetic situation of a buried Fe step. Sp-STM image of (**b**) the topography and (**d**) the corresponding spin signal of 11.9 ML Mn on Fe(001). One buried Fe step edge is running almost vertically through the center of the images, indicated by *arrows*. (**c**) Line profile taken along the *black line* in (**b**) showing a monatomic Mn step and a step of subatomic height formed by a buried Fe step. (**e**) Line profile (averaged over 70 lines) across the magnetically frustrated region in the Mn over-layer at the position of the box in (**d**). The *solid line* represents a fit to the wall profile

shows a step of monatomic height between two different Mn terraces (≈ 0.16 nm) and a step of subatomic height (≈ 0.018 nm) at the position of a buried Fe step edge due to the different lattice constants of Fe and Mn. In Fig. 4.10d clearly the layer-wise antiferromagnetic order between the Mn islands and the Mn layer underneath is visible. Following the way of the buried Fe step edge, a magnetically frustrated region is present. Along the buried Fe step edge, a reversal of the spin contrast appears. In this region the spin polarization of the Mn rotates by 180°. The observation of magnetically frustrated regions at the surface of thin Mn films at the position of buried Fe step edges indicates that the magnetic frustrations are extended throughout the whole Mn film down to the interface, as schematically shown in Fig. 4.10a. This implies that the coupling energy at the interface between Fe and Mn is higher than the domain wall energy in the Mn film which is likely for thin films. Figure 4.10e presents an averaged line profile across the topologically enforced magnetic frustration at the position of the box in Fig. 4.10d. The measurement indicates that the magnetic frustration has a certain lateral extension. To estimate the wall width at the surface, the experimental profile is fitted with a *tanh*-function and is plotted as a solid line. It reproduces the shape of the transition region well. Due to the good agreement, this function is used to determine the wall width which is in this case 4.6 ± 0.2 nm.

The width of the frustrated regions was studied as function of the Mn film thicknesses (see Fig. 4.11). The smallest width of 1.2 nm was imaged between the second and third ML Mn and the widest one of 6.9 ± 0.3 nm between 18 and 19 ML. Thicker Mn films could not be investigated due to the phase transition to α-Mn resulting in a three-dimensional growth and rough surfaces. The widening is a consequence of minimizing the exchange energy. At the interface, an atomically sharp frustration is enforced at the buried Fe step edge. This costs a maximum of magnetic exchange energy. In the layers above, the wall widens which reduces

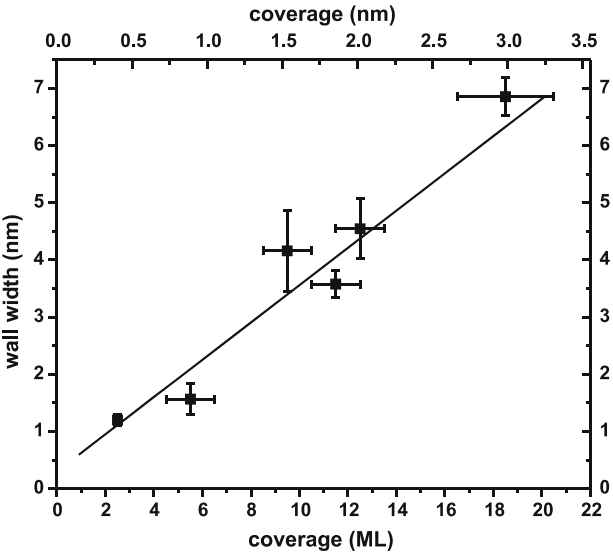

Fig. 4.11. The width of magnetically frustrated regions of Mn surface layers as a function of the Mn film thickness in ML (*bottom scale*) and equivalent in nm (*top scale*). The *solid line* is a linear fit to the experimental data points

the exchange. Eventually, the frustration reaches the bulk wall width of a 180° domain wall in Mn, which represents the energetic minimum. No further widening is expected. This limit was, however, not reached in our measurements, as we observed no sign of saturation of the width but a linear increase. We can therefore conclude, that the bulk wall width must be much larger than 7 nm [26].

4.5.2
The Layered Antiferromagnet Cr on Fe(001)

Cr(001) is a topological antiferromagnet, as already discussed in the introduction in Sect. 4.2.1. Cr can be grown pseudomorphically on Fe(001) and shows an in-plane spin polarization collinear to that of the underlying substrate [42]. We used ring electrondes aligned along the whisker axis to image the antiferromagnetic surface. Figure 4.12a shows the topography of the Cr film. Two atomic layers are exposed. As expected, the Sp-STM image recorded simultaneously shows the antiferromagetic order of the terraces (see Fig. 4.12b). The observed spin contrast is, however, only a few percent of the total tunneling current, indicating that the electronic states that are involved in the tunneling process are only weakly spin-polarized. This holds especially for tunneling conditions, where the surface state is not involved [17]. More details on the the tunneling states are discussed in Sect. 4.6.2.

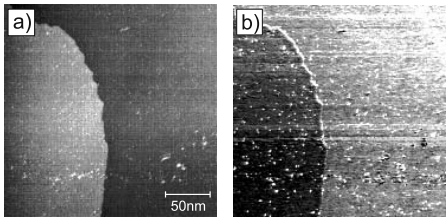

Fig. 4.12. (**a**) Topographic STM image and (**b**) magnetic Sp-STM image of the same area and (**a**) of 12.8 ML Cr on Fe(001)

4.6
Bulk Versus Surface: Which Electronic States Cause the Spin Contrast?

Analogous to STM, Sp-STM can be used to gain information of the density of states and the processes during tunneling. In contrast to STM, Sp-STM gives spin resolved information. This additional information may be used to learn more about the electronic structure of the sample and the tunneling process between the tip and the sample, itself. The capabilities of Sp-STM are illustrated with two model systems, ferromagnetic hcp Co and antiferromagnetic bcc Cr.

4.6.1
Voltage Dependence of the TMR Effect in Co(0001)

When biasing a tunneling junction by the voltage U, not only the states at the Fermi energy contribute to the tunneling current but all states between the Fermi levels of

the tip and the sample. More precisely, the tunneling current I is given by [43]:

$$I \propto \int_{E_F}^{E_F+eU} \rho_S(E)\, e^{-\frac{2d}{\hbar}\sqrt{2m\left(V_b-E+\frac{1}{2}eU\right)}} \rho_T(E-eU)\,dE \tag{4.4}$$

where ρ_S and ρ_T are the density of states of the sample and the tip. Equation (4.4) is valid for both spin channels. With this generalized Jullière model it becomes obvious that the size of the TMR should depend on the bias voltage in a way that reflects the sample and tip spin polarizations. In planar junctions, the TMR often decreases with increasing bias voltage. Due to its technological importance, many studies have been devoted to this aspect. In the early work of Jullière, a bias as small as 3 mV was needed to halve the value of the TMR. With increased control of the preparation, this value increased up to 700 mV over the years [44]. Besides the above mentioned density of states effect, several other models have been proposed to explain this behavior. Hot electrons from the positive electrode might be scattered in a spin-dependent way at defects in the amorphous barriers [45] or might create magnons [46]. These mechanisms reduce the spin polarization and, consequently, the TMR.

To pinpoint the mechanism, difficulties partly related to the complex structure of planar tunnel junctions (polycrystalline electrodes, poorly characterized amorphous barriers) have to be overcome. Here, Sp-STM measurements of the voltage dependence of the TMR across the vacuum barrier are helpful. Obviously, no effects due to impurities in the spacer are present. Magnon creation and the density-of-states effect are still present.

Measurements of the TMR were carried out in ultra-high vacuum using Sp-STM with an amorphous tip and a Co(0001) sample. During the measurement, the bias voltage was varied while keeping the tip at a fixed position and measuring the averaged tunneling current I_t and the modulated current ΔI. The TMR, defined as the asymmetry δ of the tunneling currents observed for parallel and antiparallel magnetization alignment, was obtained from I_t and ΔI. The measured TMR (Fig. 4.13a) obtained with the tip stabilized at 1 V, 1 nA is almost constant with bias voltage. This is in contrast to the case of planar tunnel junctions with amorphous spacers. If

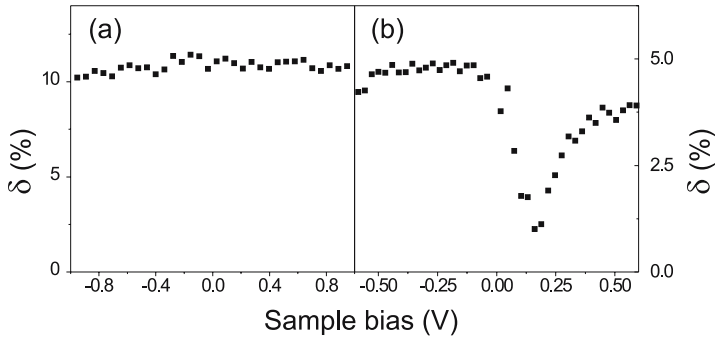

Fig. 4.13. Tunnel magneto-resistance δ of a clean Co(0001) surface versus bias voltage, obtained with a magnetic tip stabilized at 1 V, 1 nA (**a**) and at 100 mV, 1 nA (**b**)

spin-dependent scattering at magnons was the dominant mechanism for the drop of the TMR, a similar decrease of the TMR with bias voltage should also be present in our case. Its absence, however, indicates that this mechanism is not dominant. But most interestingly, the density of states effect seems to be absent as well. Both, the spin polarization of tip and sample vary strongly with energy and a variation of the TMR should be expected.

This discrepancy may be lifted easily, when having a closer look at the tunneling process. At typical tunneling conditions, the tip and sample are separated by a vacuum barrier of several atomic distances. Under these conditions, electrons with perpendicular momentum dominate the transport [8] and states with a momentum parallel to the sample plane contribute only marginal. Taking into account this effect, one may explain the constant TMR with the band structure of hcp Co along the surface normal. Figure 4.14a reveals that around the Fermi edge there is only one minority band. When assuming perpendicular tunneling, only a single band of the sample contributes to the tunneling current and no bias dependence of the TMR is expected. This interpretation was further confirmed by ab-initio calculations [47].

For small barrier widths, tunneling via surface states could become important in STM experiments [17]. This might lead to pronounced changes in the TMR. Figure 4.13b presents the experimental TMR versus bias voltage obtained at a smaller tip-sample separation (feed back conditions: 100 mV, 1 nA). For negative bias voltages, a constant TMR is still observed. For positive bias voltages, however, a strong dip at 200 mV is found. Most likely the dip is related to majority state which reduce the minority-dominated spin polarization at this energy. Indeed, inverse photoemission measurements revealed a majority surface state of Co(0001) at $\approx$ 0.2 eV [48] which is also present in the calculated layer-resolved density of states (see Fig. 4.14b). At small tip-sample separations, the tunneling probability through this surface state can be enhanced and thus would decrease significantly the TMR.

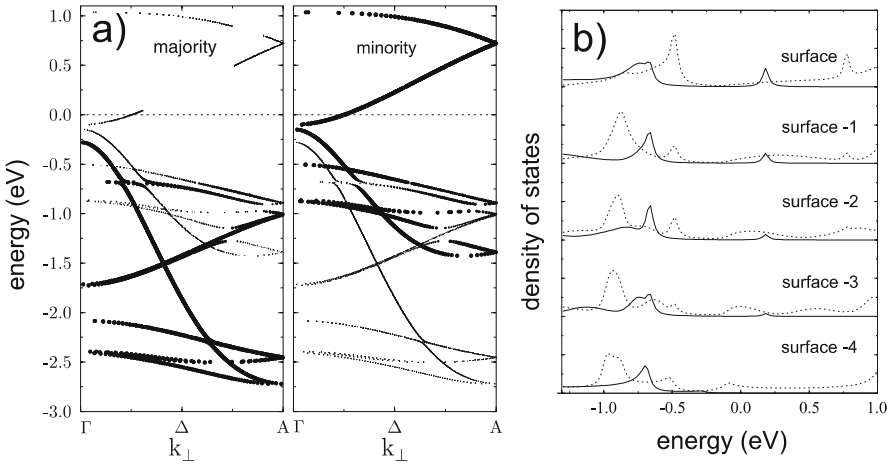

Fig. 4.14. (**a**) Theoretical spin-resolved band structure of Co(0001) along the Γ–A direction. (**b**) Theoretical spin-resolved density of states as function of distance from the surface

4.6.2
Voltage Dependence of the TMR Effect in Cr/Fe(001)

Analogous to the studies on Co(0001), the TMR as function of the bias voltage was measured for thin Cr films grown on Fe(001). Figure 4.15 shows the result for a 12 ML thick Cr film at room temperature. The overall observed spin contrast is small. This is in agreement with the fact that Cr is a layered antiferromagnet. Due to the symmetry of the magnetic order, a translation of a Cr crystal by one layer is equivalent with an inversion of the spin. This symmetry implies that the bulk states in Cr are spin polarized but spin-up and spin-down bands are degenerate. Therefore, in a tunneling experiment, no spin polarization should be caused by tunneling into the bulk states. In agreement to that, we only observe a small size of the TMR effect of about 0.65%. The non vanishing TMR is most probably related to the finite thickness of the Cr film lifting the degeneration slightly. Around the well known surface state of Cr located close to the Fermi level [49], the TMR is increased. This can be explained by tunneling into the spin polarized surface state, for which the above mentioned symmetry rules do not apply. We can therefore conclude that similar to the case of Co(0001), the tunneling current and its spin polarization is given by both bulk states and surface states. Depending on the symmetry of the states and the tunneling conditions, the balance between the two contributions to the spin polarization varies, i.e. the surface sensitivity of Sp-STM is a function of the tunneling parameters. This effect is of only minor importance in ferromagnetic films, but may become of high importance in layered systems of different electronic structure.

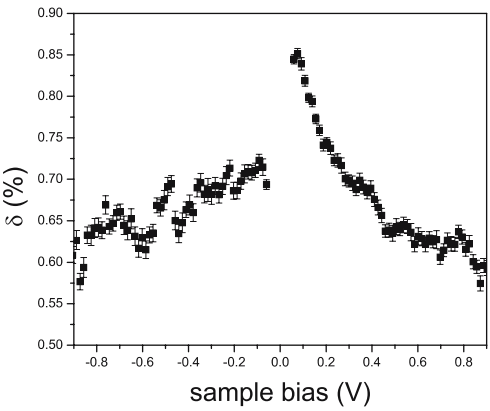

Fig. 4.15. Tunnel magneto-resistance δ of $\approx$ 12 ML Cr on Fe(001) versus bias voltage

4.7
Conclusion

With the successful operation of Sp-STM in the differential magnetic imaging mode for out-of-plane and in-plane spin polarization, Sp-STM has become an established

technique. Nevertheless, it is a young techniques and future studies on ferromagnetic and antiferromagnetic systems will give a deeper understanding of magnetism on the nanometer scale. For antiferromagnets, the real space information gained is complementary to the information already available from magnetic scattering techniques like neutron scattering. Sp-STM allows to tackle the new class of problems in antiferromagnets: frustrations and aperiodic structures. Finally, Sp-STM may be used to investigate the density of states and its spin polarization via the processes of spin-polarized tunneling. By this, it has the potential to become a valuable tool for electron spectroscopy.

References

1. Barkhausen H (1919) Phys Z 50:401
2. Hopster H, Oepen HP (2004) Magnetic Microscopy of Nanostructures, Springer, Berlin Heidelberg New York
3. Tersoff J, Hamann DR (1983) Phys Rev Lett 50:1998
4. Tersoff J, Hamann DR (1985) Phys Rev B 31:805
5. Müller N, Eckstein W, Heiland W, Zinn W (1972) Phys Rev Lett 29:1651
6. Landolt M, Yafet Y (1978) Phys Rev Lett 40:1401
7. Jullière M (1975) Phys Lett 54A:225
8. Slonczewski JC (1989) Phys Rev B 39:6995
9. Miyazaki T, Tezuka N (1995) J Magn Magn Mater 139:L231
10. Binning G, Rohrer H, Gerber Ch, Weibel E (1982) Appl Phys Lett 40:178
11. Binning G, Rohrer H, Gerber Ch, Weibel E (1982) Phys Rev Lett 49:57
12. Pierce DT (1988) Physica Scripta 38:291
13. Suzuki Y, Nabhan W, Tanaka K (1997) Appl Phys Lett 71:3153
14. Heinze S, Kurz P, Wortmann D, Bihlmayer G, Blügel S (2002) Appl Phys A 75:25
15. Wiesendanger R, Güntherodt HJ, Güntherodt G, Gambino RJ, Ruf R (1990) Phys Rev Lett 65:247
16. Blügel S, Pescia D, Dederichs PH (1989) Phys Rev B 39:1392
17. Stroscio JA, Pierce DT, Davies A, Celotta RJ, Weinert M (1995) Phys Rev Lett 75:2960
18. Bode M, Getzlaff M, Wiesendanger R (1998) Phys Rev Lett 81:4256
19. Kubetzka A, Bode M, Pietzsch O, Wiesendanger R (2002) Phys Rev Lett 88:057201
20. Yamada TK, Bischoff MMJ, Heijnen GMM, Mizoguchi T, van Kempen H (2003) Phys Rev Lett 90:056803
21. Wulfhekel W, Kirschner J (1999) Appl Phys Lett 75:1944
22. Johnson M, Clarke J (1990) J Appl Phys 67:6141
23. Ding HF, Wulfhekel W, Kirschner J (2002) Europhys Lett 57:100
24. Schlickum U, Wulfhekel W, Kirschner J (2003) Appl Phys Lett 83:2016
25. Wulfhekel W, Hertel R, Ding HF, Steierl G, Kirschner J (2002) J Magn Magn Mater 249:368
26. Schlickum U, Janke-Gilman N, Wulfhekel W, Kirschner J (2004) Phys Rev Lett 92:107203
27. Unguris J, Scheinfein MR, Celotta RC, Pierce DT (1989) Appl Phys Lett 55:2553
28. Hubert A, Schäfer R (1998) Magnetic Domains, Springer-Verlag, Berlin, pp 315
29. Scheinfein MR, Unguris J, Blue JL, Coakley KJ, Pierce DT, Celotta RJ (1991) Phys Rev B 43:3395
30. Heinrich B, Arrott AS, Liu C, Purcell ST (1987) J Vac Sci Technol A 5:1935
31. Purcell ST, Johnson MT, McGee NWE, Coehoorn R, Hoving W (1992) Phys Rev B 45:13064
32. Kim SK, Tian Y, Montesano M, Jona F, Marcus PM (1996) Phys Rev B 54:5081
33. Andrieu S, Foy E, Fischer H, Alnot M, Chevrier F, Krill G, Piecuch M (1998) Phys Rev B 58:8210

34. Tulchinsky DA, Unguris J, Celotta RJ (2000) J Magn Magn Mater 212:91
35. Pfandzelter R, Igel T, Winter H (1997) Surf Sci 389:317
36. Pierce DT, Davies AD, Stroscio JA, Tulchinsky DA, Unguris J, Celotta RJ (2000) J Magn Magn Mater 222:13
37. Yamada TK, Bischoff MMJ, Mizoguchi T, van Kempen H (2002) Surf Sci 516:179
38. Walker TG, Hopster H (1993) Phys Rev B 48:3563
39. Bischoff MMJ, Yamada T, Quinn AJ, van Kempen H (2002) Surf Sci 501:155
40. Berger A, Hopster H (1994) Phys Rev Lett 73:193
41. Berger A, Fullerton EE (1997) J Magn Magn Mater 165:471
42. Pierce DT, Unguris J, Celotta RJ, Stiles MD (1999) J Magn Magn Mater 200:290
43. Lang ND (1986) Phys Rev B 34:5947
44. Boeve H, Girgis E, Schelten J, De Boeck J, Borghs G (2000) Appl Phys Lett 76:1048
45. Zhang J, White R (1998) J Appl Phys 83:6512
46. Moodera JS, Nowak J, van de Veerdonk RJM (1998) Phys Rev Lett 80:2941
47. Ding HF, Wulfhekel W, Henk J, Bruno P, Kirschner J (2003) Phys Rev Lett 90:116603
48. Math C et al (2001) Surf Sci 482-485:556
49. Kleiber M, Bode M, Ravlic R, Wiesendanger R (2000) Phys Rev Lett 85:4606